POLITECNICO DI TORINO
Repository ISTITUZIONALE

3D printed lattice metal structures for enhanced heat transfer in latent heat storage systems

Original
3D printed lattice metal structures for enhanced heat transfer in latent heat storage systems / Morciano, M., Fasano, M., Calignano, F., Manfredi, D.G., Asinari, P., Chiavazzo, E., Alberghini, M., Almiento, M.. - In: JOURNAL OF ENERGY STORAGE. - ISSN 2352-152X. - 65:(2023), pp. 1-10. [10.1016/j.est.2023.107350]

Availability:
This version is available at: 11583/2978083 since: 2023-04-20T15:19:25Z

Publisher:
Elsevier

Published
DOI:10.1016/j.est.2023.107350

Terms of use:

This article is made available under terms and conditions as specified in the corresponding bibliographic description in the repository

Publisher copyright

(Article begins on next page)

09 November 2026

Journal of Energy Storage 65 (2023) 107350

Contents lists available at ScienceDirect

Journal of Energy Storage

journal homepage: www.elsevier.com/locate/est

Research papers

3D printed lattice metal structures for enhanced heat transfer in latent heat storage systems

Matteo Morciano [a,b,1], Matteo Alberghini [a,b,1], Matteo Fasano [a,b], Mariella Almiento [a], Flaviana Calignano [c], Diego Manfredi [d], Pietro Asinari [a,e], Eliodoro Chiavazzo [a,b,*]

[a] Department of Energy, Politecnico di Torino, Corso Duca degli Abruzzi 24, 10129 Torino, Italy
[b] Clean Water Center, Corso Duca degli Abruzzi 24, Torino, Italy
[c] Department of Management and Production Engineering, Politecnico di Torino, Corso Duca degli Abruzzi 24, 10129 Torino, Italy
[d] Department of Applied Science and Technology, Politecnico di Torino, Corso Duca degli Abruzzi 24, 10129 Turin, Italy
[e] INRIM, Istituto Nazionale di Ricerca Metrologica, Strada delle Cacce 91, Torino, Italy

ARTICLE INFO

Keywords:
Thermal energy storage
Phase change materials
Additive manufacturing
3D printing
Enhanced heat transfer

ABSTRACT

The low thermal conductivity of Phase Change Materials (PCMs), e.g., paraffin waxes, is one of the main drawbacks of latent heat storage, especially when fast charging and discharging cycles are required. The introduction of highly conductive fillers in the PCM matrix may be an effective solution; however, it is difficult to grant their stable and homogeneous dispersion, which therefore limits the resulting enhancement of the overall thermal conductivity. Metal 3D printing or additive manufacturing, instead, allows to manufacture complex geometries with precise patterns, therefore allowing the design of optimal paths for heat conduction within the PCM. In this work, a device-scale latent heat storage system operating at medium temperatures (~ 90 °C) was manufactured and characterized. Its innovative design relies on a 3D Cartesian metal lattice, fabricated via laser powder bed fusion, to achieve higher specific power densities. Numerical and experimental tests demonstrated remarkable specific power (approximately 714 ± 17 W kg^{-1} and 1310 ± 48 W kg^{-1} during heat charge and discharge, respectively). Moreover, the device performance remained stable over multiple charging and discharging cycles. Finally, simulation results were used to infer general design guidelines to further enhance the device performance. This work aims at promoting the use of metal additive manufacturing to design efficient and responsive thermal energy storage units for medium-sized applications, such as in the automotive sector (e.g. speed up of the engine warm up or as an auxiliary for other enhanced thermal management strategies).

1. Introduction

Thermal energy storage (TES) plays a fundamental role in increasing the sustainability of a broad variety of sectors, for example the solar [1–3] or automotive [4,5] industries, since it allows to efficiently exploit heat sources with intermittent availability.

In particular, latent TES is based on the thermal energy released (or absorbed) when a material undergoes phase change [6]. Latent TES has generally superior performance than sensible one, since it allows to store a larger amount of energy (*i.e.* higher energy density) at nearly constant temperature, with the potential to precisely control the heat release process [7,8]. Different Phase Change Materials (PCMs) are currently available, according to the specific operating condition of the TES system. Paraffins (alkanes) are typically employed as far as medium temperatures are concerned. Paraffin waxes are straight hydrocarbon chains of type $CH_3(CH_2)_nCH_3$ with a wide range of melting temperatures (0 °C – 80 °C [9]), being characterized by excellent durability over multiple thermal cycles. However, paraffin waxes present low values of thermal conductivity limiting their specific power (W kg^{-1}). As a result, the time required for thermal charging and discharging increases.

Previous works showed different ways to overcome this issue, e.g., with the use of PCM cascades [10], addition of fins [2,11–13], micro- [14,15] or macro-encapsulations [16]. In particular, high thermal conductivity enhancements were observed after the inclusion of highly conductive compounds in the PCM matrix, such as graphite nano-components [17–22] or foams [2,3,23–25]. Worth mentioning, by way of example, Liu and co-workers have recently designed and proposed a novel hybrid metal foam-pin fin structure [2], with the aim of improving the energy efficiency of solar-aided thermal storage

* Corresponding author at: Department of Energy, Politecnico di Torino, Corso Duca degli Abruzzi 24, 10129 Torino, Italy.
E-mail address: eliodoro.chiavazzo@polito.it (E. Chiavazzo).
[1] Shared first authorship.

https://doi.org/10.1016/j.est.2023.107350
Received 26 September 2022; Received in revised form 28 March 2023; Accepted 3 April 2023
Available online 14 April 2023
2352-152X/© 2023 The Authors. Published by Elsevier Ltd. This is an open access article under the CC BY license (http://creativecommons.org/licenses/by/4.0/).

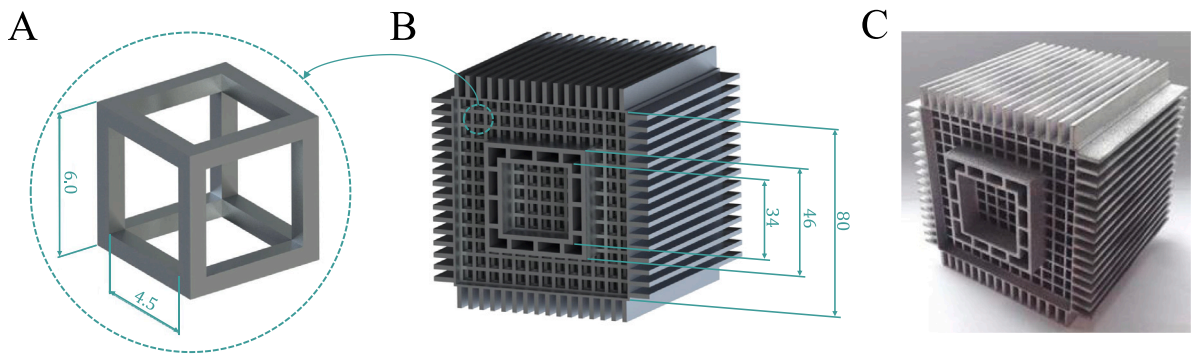

Fig. 1. Design of the heat storage prototype. (A) Single hollow cubic element used to create the ordered Cartesian lattice. (B) 3D CAD model of the device realized. A STL file of the device can be downloaded from the Supplementary Material. All the quotes are expressed in mm. (C) Picture of the realized prototype.

applications, and a novel energy storage tank filled by phase change materials with graded metal foams [3] to further improve melting/solidification efficiency. In addition, Xiao and co-workers have designed a novel latent heat thermal storage tank with multi-channels filled with metal foams, reducing by 23.7% the transition time, compared with the non porous tank [26]. However, the dispersion of conductive fillers in the matrix is hardly controllable and, thus, non-optimized dispersions of fillers may limit the achievable effective thermal conductivity [27]. On the other hand, the inclusion of 2D metal grids with optimized geometry within the paraffin matrix has shown promising heat transfer enhancements [28–31]. Metal additive manufacturing has the potential to further extend this concept, since it allows to produce complex 3D structures with high porosity, namely large surface-to-volume ratio [32–37].

In this article, metal additive manufacturing was used to produce a 3D Cartesian metal lattice to enhance the performance of a latent heat storage system, which was designed to work with paraffin waxes characterized by fusion temperatures of ~80 °C. Numerical simulations and experimental tests were performed to investigate the thermal performance of the prototype in terms of energy stored and released, characteristic time of charge and discharge, and power density. In detail, remarkable specific powers of approximately 714 ± 17 W kg^{-1} and 1310 ± 48 W kg^{-1} were accomplished during heat charge and discharge, respectively. Furthermore, the performance of the device was stable for repeated charging and discharging cycles. The manufactured TES unit was envisaged for use in automotive applications, with the aim of recovering, storing and re-using the waste-heat from the engine cooling system to speed up the cold-start phase, which is critical for the production of pollutants [38]. The article is organized as follows. First, the prototype design, fabrication, and testing procedures are reported in Section 2.1. Second, the finite elements model implemented, representing the device and the testing conditions, is described in Section 2.2. Third, the experimental results obtained were used to validate the numerical model, which was then employed to gain further insight of the device performance, reported in Section 3. Finally, conclusions and future perspectives are discussed in Section 4.

2. Materials and methods

2.1. Device fabrication and testing procedure

The innovative latent TES system investigated was designed to achieve short characteristic times of thermal charge and discharge. For this purpose, a 3-dimensional metal structure was fabricated via laser powder bed fusion (L-PBF) and then infiltrated by paraffin wax. In this way, the high thermal conductivity of the metal lattice was used to homogenize the temperature of the PCM matrix and, simultaneously, decrease its melting and solidification time. At the same time, the metal

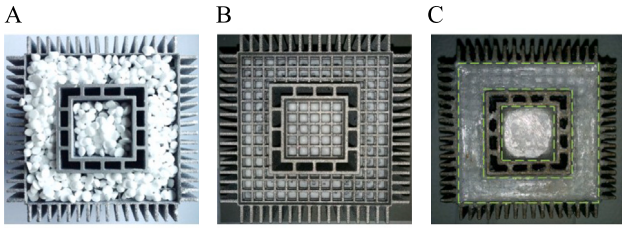

Fig. 2. Filling procedure of the 3D Cartesian lattice with the PCM. The wax chips were weighted and placed within the prototype (A), melted (B) and sealed (C) via an acrylic glass cover (delimited by green dashed lines in the figure). (For interpretation of the references to color in this figure legend, the reader is referred to the web version of this article.)

lattice was also conceived to perform as heat exchanger between a heat-transfer fluid (HTF) and the TES system.

The designed metal structure has cubic shape (80 mm × 80 mm × 80 mm) with an internal Cartesian lattice consisting of the repetition of identical hollow cubic elements (6 mm side) (see Fig. 1A). The HTF flows through both a inner duct (inner side 34 mm; outer side 46 mm, see Fig. 1B) and fins (3 mm thick, 9 mm long) placed on the external surface of device. The 3D Cartesian lattice was fabricated via L-PBF of an aluminum alloy AlSi10Mg (EOS) powder bed [39–41]. This technique allows to manufacture layer-by-layer complex-shaped components by melting metal powders with a laser beam [42]. The resulting device is shown in Fig. 1C and is characterized by a mass of approximately 630 g and a porosity of 71%, the latter being defined as the empty volume fraction within the Cartesian lattice. An EOSINT M270 Dual-mode system has been used to build the AlSi10Mg components. This machine is equipped with a 200 W Yb-fiber laser. During the manufacturing process, the building chamber is filled with an inert gas (argon) in order to keep the oxygen content less than 0.10%. Details of the L-PBF manufacturing process parameters are reported in [42]. The orientation of the component on the build platform is chosen as to make the surfaces of the internal channel self-supporting. Then, approximately 280 g of paraffin wax were infiltrated through the metal lattice and sealed by two acrylic glass gaskets (see Fig. 2). A wood cover (128 mm × 128 mm × 128 mm) was used to enclose the device and contain the HTF flowing across the external fins. Finally, the prototype and the hydraulic circuits were coated by 5 mm of mineral wool to improve thermal insulation with the surrounding environment.

A schematic of the test bench used to investigate the performance of the TES system is reported in Fig. 3, comprising a 20 L water tank, a electric heater (3 kW, RS Pro), a volumetric pump (Xylem Flojet 083942), three type K thermocouples (Class 1, RS Pro), and a DAQ system (National Instruments). First, the water contained in the tank was heated up by the electric heater and recirculated by the volumetric pump until the desired inlet temperature was reached

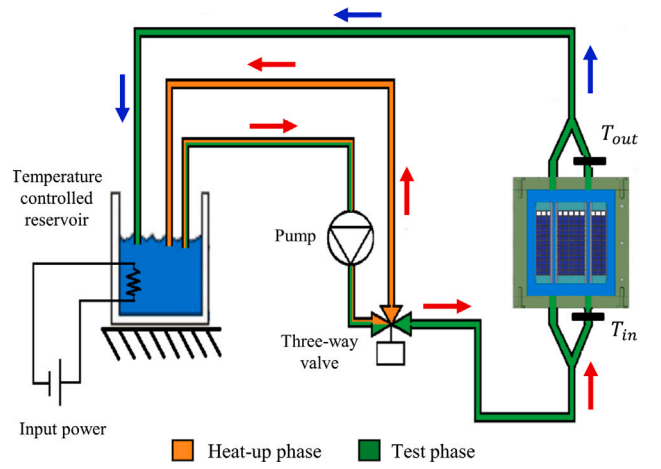

Fig. 3. Schematic of the experimental setup used to test the thermal energy storage device. The heat storage characterization is subdivided into three phases. First, the tank is heated up to the desired inlet temperature (heating phase, orange circuit). Second, the heat-transfer fluid is deviated towards the device, melting the PCM (charging phase, green circuit). Finally, the PCM is solidified by setting the heat-transfer fluid inlet temperature equal to the ambient one (discharging phase, green circuit). (For interpretation of the references to color in this figure legend, the reader is referred to the web version of this article.)

(heating phase, represented in orange in Fig. 3). Second, a three-way valve was activated, deviating the hot water towards the prototype and then back to the tank (charging phase, represented in green in Fig. 3). Two type K thermocouples were used to evaluate the water temperature at the inlet and outlet sections of the prototype (T_{in} and T_{out}, respectively), while a third one was used to measure the ambient temperature. Third, the discharging phase was tested by setting the inlet temperature equal to the ambient temperature. The DAQ system was employed to acquire the three temperature signals. The typical temperature range of the HTF (e.g. engine coolant) varies in the range 60–90 °C for automotive TES systems. Therefore, a paraffin wax with melting temperature of about 70 °C (RT70HC, Rubitherm) was selected. The mass flow rate of the HTF was set to 3.3 L min^{-1}.

2.2. Finite elements model

A three-dimensional model, representative of the TES device, was implemented via the finite elements software (FEM) COMSOL Multiphysics (see Fig. 4). The computational cost was reduced relying on the geometrical symmetries of the system, thus representing only 1/8 of the device [43]. The simulations were performed solving the energy equation in all the computational domain:

$$\rho c_p \frac{\partial T}{\partial t} + \rho c_p \mathbf{v} \cdot \nabla T - k\nabla^2 T = 0\,, \tag{1}$$

where ρ, k and c_p are the density, thermal conductivity and specific heat capacity of the material considered, T is the temperature and $\mathbf{v}$ is the velocity field. Note that Eq. (1) was formulated neglecting the effect of external or internal volumetric heat sources. Fluid flow was only considered within the channels filled by the HTF and modeled in the form:

$$\rho \frac{\partial \mathbf{v}}{\partial t} = -\nabla p + \mu \nabla^2 \mathbf{v} + \rho g\,, \tag{2}$$

where p is the fluid pressure and μ its dynamic viscosity, g is the gravitational acceleration and the contribution of the inertial term is neglected.

Referring to the schematic reported in Fig. 4, the HTF (water) was supposed to flow bottom-up at constant and perpendicular inlet velocity 0.023 m s^{-1} with fixed upstream temperature, while the outlet section was considered to remain at ambient pressure. The temperature of the metal lattice surfaces adjacent to the HTF inlet was considered as fixed and equal to that of the upstream flow. Convective heat losses were modeled on the outer faces of the wood and wool insulation layers by means of a convective heat transfer coefficient of 6 W m^{-2} K^{-1}, while the remaining surfaces of the setup were supposed to be either perfectly insulated or belonging to a symmetry plane. The PCM was considered as a solid even upon complete melting due its high viscosity and small separations between the cubic elements; therefore, the effect of convection (second term in Eq. (1)) was neglected except for the HTF. Finally, to comply with the experimental testing conditions, the upstream inlet temperature of the HTF was evaluated via cubic interpolation of the temperature signals acquired.

Table 1
Material-dependent coefficients of Eq. (3) optimized for the apparent specific heat capacity c_p^a of the paraffin RT70HC during fusion and solidification.

	Fusion	Solidification
c_0 (kJ kg^{-1} K^{-1})	2	2
p_1 (kJ kg^{-1} K^{-1})	0	71 ± 13
σ_1 (–)	–	0.54 ± 0.09
p_2 (kJ kg^{-1} K^{-1})	207.8 ± 14.5	124.5 ± 19.7
σ_2 (–)	0.560 ± 0.03	0.414 ± 0.06

To reduce the computational cost, Eq. (2) was solved only for the first 15 s of the charging process, while the remaining part of the simulation was performed considering the velocity profile evaluated at 15 s as constant. The stability of the velocity field was evaluated by monitoring the time evolution of the zero-norm of the velocity residuals within the HTF. The results obtained show that the velocity field does not present significant changes after 10 s despite the progressive increase of the average fluid temperature. Then, coherently with the experimental characterization, the simulations of the discharging process were performed considering a steady fluid flow, therefore assuming the velocity field as unchanged with respect to the charging phase.

The fusion and solidification of the paraffin wax were modeled via the apparent specific heat capacity method [44], which models the latent heat as a temperature-dependent function presenting peaks at the characteristic temperatures of phase change, to be added to the specific heat capacity. The peaks were described by Gaussian functions, whose integrals with respect to temperature yield the latent heat of the PCM. The apparent specific heat capacity c_p^a, expressed in kJ kg^{-1} K^{-1}, was evaluated by fitting the experimental data reported by the PCM manufacturer (see Ref. [45]) in the form:

$$\begin{aligned} c_p^a &= c_0 + p_1 G(T, T_1^{pc}, \sigma_1) + p_2 G(T, T_2^{pc}, \sigma_2) \\ G(x, \bar{x}, \sigma) &= \frac{1}{\sigma\sqrt{2\pi}} \exp\left(-\frac{(x-\bar{x})^2}{2\sigma^2}\right), \end{aligned} \tag{3}$$

where c_0, $p_{1/2}$ and $\sigma_{1/2}$ are material-dependent parameters fitted on experimental data, T_1^{pc} = 67 °C and T_2^{pc} = 70 °C are the characteristic phase change temperatures of the PCM considered (see Ref. [45]), T is expressed in °C, and G is a Gaussian function of x centered in $\bar{x}$ with standard deviation σ. Note that c_0 represents the specific heat capacity of the wax in both solid and liquid states. The experimental data of the paraffin wax RT70HC and the resulting fitting curves are reported in Fig. 5, while the optimized material-dependent parameters are reported in Table 1. Similarly, the variation of density ρ between the solid and melted PCM was evaluated via a smoothed step function, which provides a continuous variation between the solid (ρ = 880 kg m^{-3}) and liquid (ρ = 770 kg m^{-3}) density values as reported in Ref. [45], considering the temperature range $T_2^{pc} \pm \sigma_2$ for the phase transition.

The temperature-dependent thermo-physical properties of water were evaluated via the built-in libraries of the FEM software used; whereas the remaining parameters of the considered materials, comprising the specific heat capacity c_p, thermal conductivity k and density

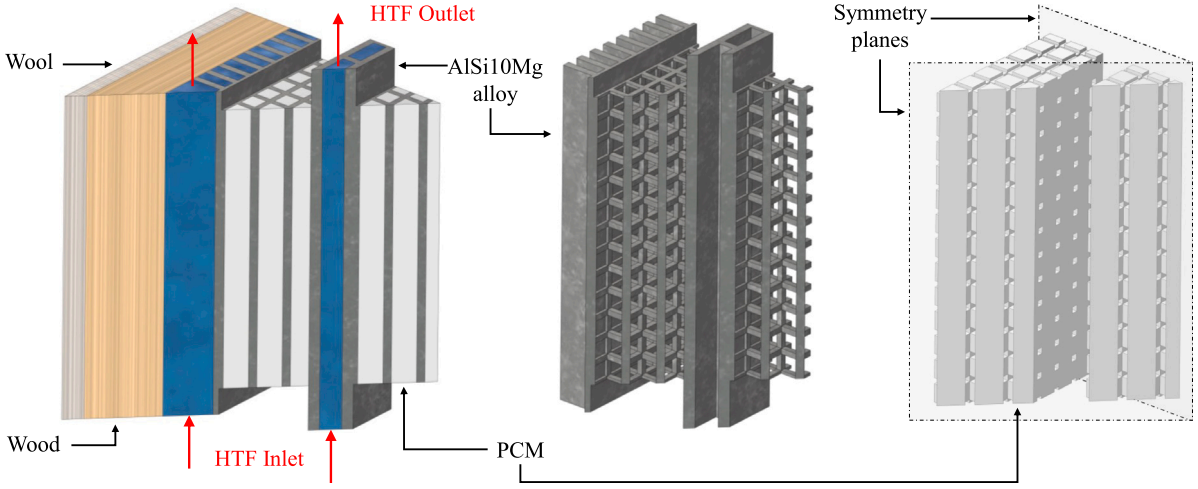

Fig. 4. 3-dimensional computational model. Representative computational domain of the TES device manufactured simulating the tested charging and discharging processes, highlighting its main features and materials used. To reduce the computational cost, geometrical symmetries were used to simulate only 1/8 of the device.

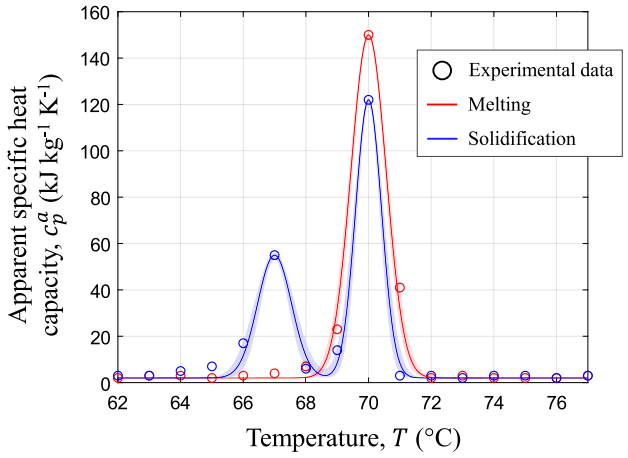

Fig. 5. Apparent specific heat capacity of the considered PCM. Experimental data (circles) and fitting curves (solid lines) of the apparent specific heat capacity c_p^a for melting (red data) and solidification (blue data). The experimental data were retrieved from Ref. [45], while Eq. (3) and the coefficients reported in Table 1 were used to obtain the reported curves. The shaded areas represent the uncertainty of the fitting curves, obtained considering the data reported in Table 1. (For interpretation of the references to color in this figure legend, the reader is referred to the web version of this article.)

Table 2
Temperature-independent material properties employed to implement the numerical model.

	Aluminum	Wood	Mineral wool
c_p (kJ kg^{-1} K^{-1})	0.92	1.6	1.3
k (W m^{-1} K^{-1})	140	0.11	0.04
ρ (kg m^{-3})	2400	490	1315

ρ are reported in Table 2. A detailed discussion of the aluminum alloy properties is reported in Refs. [39–41].

To ensure a correct representation of the prototype tested, it was verified that the mass of the simulated device m_{tot}, comprising the PCM and the metal lattice, was consistent with the experimental values. Considering the system symmetries, the masses of the simulated PCM and aluminum domains were 283 g and 630 g, respectively, both coherent with the reported experimental values (see Section 2.1).

The thermal performance of the device was evaluated in terms of the total (E) and latent (L) heat stored or released during the process. The former was evaluated considering both the volumes of the PCM and metal lattice (V_{pcm} and V_{al}, respectively) as:

$$E = \int_{V_{pcm}} \left(\int_{T_0}^{T} \rho_{pcm}(T)\, c_p^a(T)\, dT \right) dV + \int_{V_{al}} \left(\int_{T_0}^{T} \rho_{al} c_{p,al}\, dT \right) dV , \tag{4}$$

where c_p^a is the apparent specific heat capacity evaluated from Eq. (3), $c_{p,al}$ is the specific heat capacity of the aluminum lattice (see Table 2), and T_0 is the initial temperature at the beginning of the charging or discharging process. Similarly, the latent heat stored or released L by the PCM was evaluated as:

$$L = \int_{V_{pcm}} \left(\int_{T_0}^{T} \rho_{pcm}(T) \left(c_p^a(T) - c_0 \right) dT \right) dV . \tag{5}$$

Finally, the percentage of melted or solidified PCM during the charging or discharging process was evaluated as:

$$\alpha = \frac{1}{V_{pcm}} \int_{V_{pcm}} \delta\, dV , \tag{6}$$

where the parameter δ was evaluated as:

$$\delta = \begin{cases} 0 & \text{if } T \le T_f^{pc} \\ 1 & \text{if } T > T_f^{pc} \end{cases} , \tag{7}$$

where T_r^{pc} is the final phase change temperature, with $T_r^{pc} = T_2^{pc} + 2\sigma_2$ for fusion and $T_r^{pc} = T_1^{pc} - 2\sigma_1$ for solidification.

The mismatch between experimental and numerical results was evaluated via the normalized root mean squared error (nRMSE) as:

$$nRMSE = \frac{1}{\max(T^{exp})} \left(\frac{\sum_{i=1}^{N} \left(T_i^{exp} - T_i^{sim} \right)^2}{N} \right)^{0.5} , \tag{8}$$

where T^{exp} and T^{sim} are the experimental and simulated temperatures, respectively, both evaluated at the same i-th time-step, and N is the total number of time-steps considered. Finally, the numerical model was successfully tested for mesh convergence.

3. Results

The charging and discharging processes of the manufactured device were tested both experimentally and numerically. In particular, the experimental results were used to validate the FEM model, which was then employed to gain further insight on the melting and solidification transients within the Cartesian metal lattice. The tests were performed

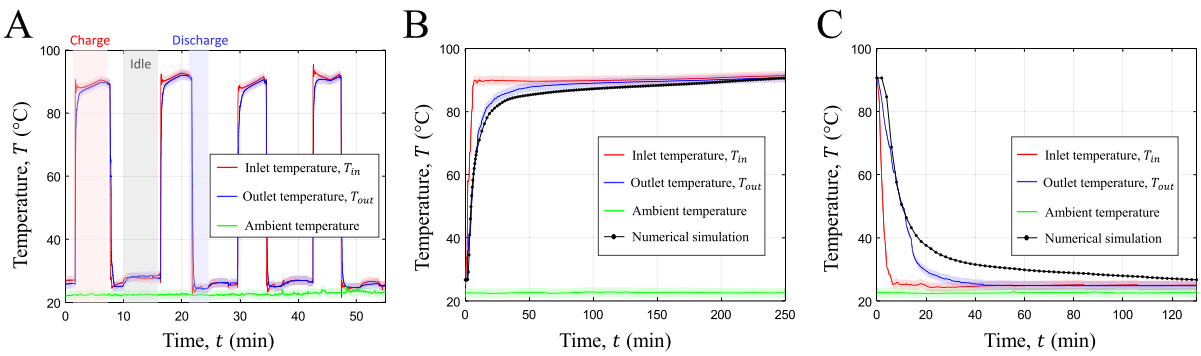

Fig. 6. Thermal energy storage performance of the device: experimental results and validation of numerical model. (A) Charging (red background) and discharging (blue background) cycles of the TES prototype, replicated at regular intervals of time (gray background). Solid red and blue curves represent inlet and outlet water temperatures, respectively, while the solid green curve represents the ambient temperature. (B–C) Validation of the numerical model. The experimental outlet temperatures (solid blue lines) during the charging (B) and discharging (C) transients were compared with the numerical results (dotted black lines). The shaded area of each temperature curve represents its uncertainty. (For interpretation of the references to color in this figure legend, the reader is referred to the web version of this article.)

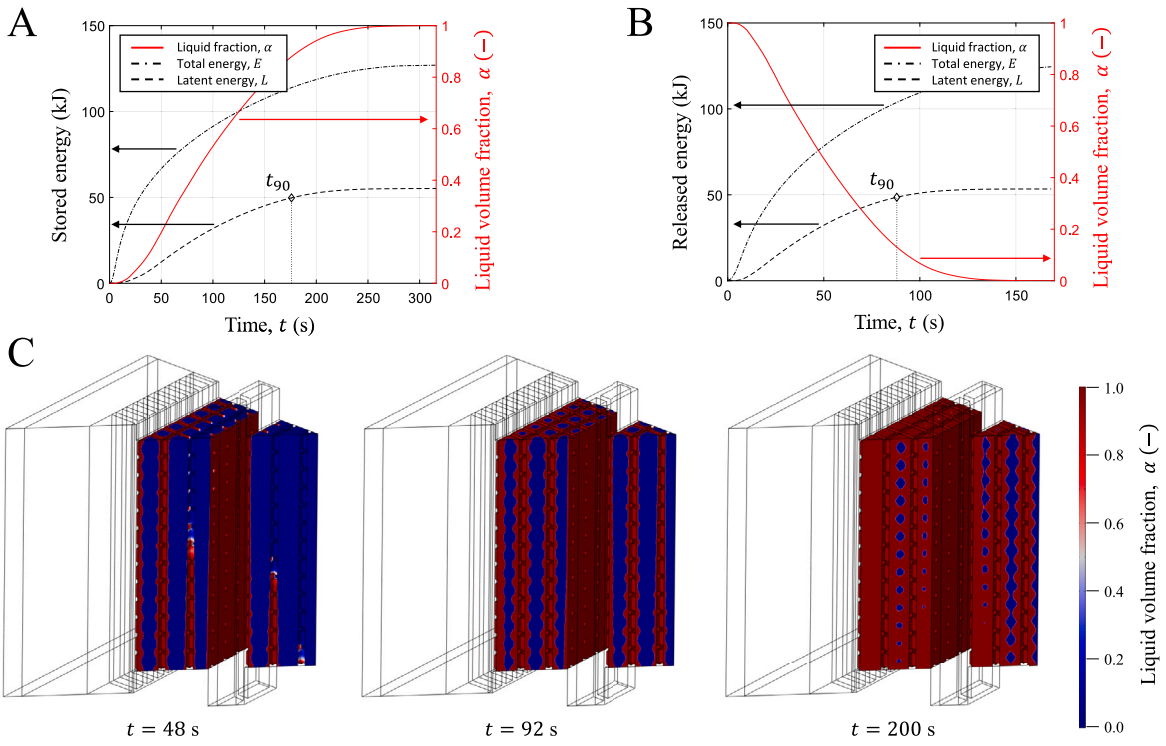

Fig. 7. Thermal energy storage performance of the device: numerical results. Analysis of the percentage of the melted volume of PCM (α, red data) and thermal energy stored (A) or released (B) during the charging and discharging phases. Simulation results show that the tested conditions lead to faster solidification rather than melting. (C) Liquid volume fraction α of the PCM during the simulated charging process at different time frames.

considering inlet temperature set points of 90 °C and 24 °C for the charging and discharging processes, respectively. Note that the tests were carried out under controlled laboratory conditions, with ambient temperature fixed at (22.5 ± 1.5) °C.

Four sequential charging and discharging cycles were performed in sequence to assess the stability of the prototype performance (see Fig. 6A), where each charge (red-shaded area) and discharge (blue-shaded area) was followed by a idle (gray-shaded area) period to ensure homogeneous temperature throughout the whole device. The results of each test were averaged to obtain representative temperature curves for the charging and the discharging processes relative to the tested operating conditions (see red and blue curves in Fig. 6B–C for the inlet and outlet temperatures, respectively). The resulting experimental curves of the outlet fluid temperature (blue data) were employed to validate the numerical results obtained via the FEM model. Note that the simulations were performed considering as upstream temperature of the HTF the respective experimental curves (red data). The temperature curves obtained via numerical simulations (dotted black data) show good agreement with the experimental ones: a nRMSE of 2.2% and 5.4% were obtained for the charging and discharging processes, respectively, via Eq. (8). A potential reason behind the reported, but acceptable, discrepancy between the experimental and numerical temperature profiles may lie in the non-ideal contact between the paraffin wax and the metal structure arising from the shrinkage of the volume of material being solidified.

The amount of thermal energy stored and then released E was evaluated via Eq. (4), considering T_0 = 26.6 °C and T_0 = 91.3 °C for the charging and discharging processes, respectively, coherently with the experimental data. As a result, the validated simulations show that the device stored and released ~125 kJ, for an overall energy density of nearly 140 kJ kg^{-1}. Interestingly, approximately 35% of the energy stored and released can be ascribed to latent heat, evaluated via

Table 3
Sensible and latent heat contributions during the charging and discharging phases.

	Charge	Discharge
PCM - Latent	39.5%	31.8%
PCM - Sensible	24.9%	20.2%
Aluminum	26.6%	22.2%
Wood	8.6%	14.3%
Mineral wool	0.4%	11.5%

Eq. (5), while the contribution of sensible heat due to the aluminum matrix contributes with less than 25% of the total energy stored or released (see Table 3 for details on the various latent and sensible heat contributions). This result highlights the effectiveness of coupling latent and sensible thermal energy storage mechanisms, accumulating larger amounts of energy without requiring higher HTF temperatures. On the other hand, higher HTF temperatures would lead to increased E (i.e., more sensible heat stored) but, at the same time, would increase the thermal losses during the storage period. Furthermore, note that the phase-change temperature of the selected PCM sets a lower limit to the HTF inlet temperature. Consequently, the PCM should be selected with the aim of maximizing the latent heat stored and, at the same time, improving the overall efficiency of the system. As an example, the optimal phase exchange temperature can be identified as that which maximizes the exergy of the charging process, which can be evaluated as suggested by Bjurström and co-worker [46]:

$$T_{opt} = \sqrt{T_{in} T_{ref}}\,, \tag{9}$$

which, considering the working parameters selected $T_{in} = 90$ °C and $T_{ref} = T_{amb} = 22.5$ °C, results in $T_2^{pc} = T_{opt} = 54.5$ °C.

An important parameter defining the performance of the device is the characteristic time required to store or release 90% of the available latent heat L, namely t_{90}. Clearly, lower values of t_{90} lead to a faster response of the TES unit. Values of t_{90} for charge and discharge were accurately evaluated through the numerical results, obtaining $t_{90} = (176 \pm 4)$ s and $t_{90} = (88 \pm 3)$ s for the charging and discharging phases (black diamonds reported in Fig. 7A–B). These values are in good agreement with the typical short transient required in the automotive field [47]. Note that the temperature difference between the phase change temperature of the PCM (~70 °C) and the inlet temperature of the HTF during melting is about half of that during solidification, which justifies the difference between the characteristic times of the two tested transients.

In this regard, the most interesting figure of merit of the manufactured heat storage device can be expressed in terms of power density SP, namely:

$$SP = \frac{E_{90}}{t_{90} \cdot m_{tot}}\,, \tag{10}$$

where E_{90} was evaluated via Eq. (4) at t_{90} and $m_{tot} = 913$ g is the overall mass of the storage device, comprising both the PCM and the metal structure. Results show remarkable values of power density, between $SP = (714 \pm 17)$ W kg^{-1} and $SP = (1310 \pm 48)$ W kg^{-1} for the charging and discharging processes, respectively.

The results of the simulations were used to infer optimal design strategies for improving the performance of 3D Cartesian lattices akin to the one realized. The melting process of the PCM within the device can be analyzed in terms of the time evolution of the liquid volume fraction α (see Fig. 7C). As it can be observed, the PCM near the HTF channels was melted after approximately 50 s; consistently, the difference between the experimental temperature curves measured at the inlet and outlet sections of the device became statistically negligible after about 50 s of testing (see Fig. 6B). However, at this stage only 20% of the PCM was melted (see Fig. 7A). After about 90 s, the PCM surrounding the metal lattice was entirely melted, corresponding only to $\alpha \sim 50\%$. Since other 200 s were necessary to achieve complete fusion (namely, $\alpha = 1$), the remaining part of the process was driven by the thermal diffusion within the PCM, which, being poorly conductive, limits the heat transfer performance of the device. This analysis suggests that faster melting transients can be pursued by increasing the surface-to-volume ratio of the Cartesian lattice, which can be achieved, for example, by decreasing the size of the elementary cells (see the schematic in Fig. 1A). This would clearly lead to an increase in the mass of the metal lattice, resulting in increased fabrication time and cost. Since both t_{90} and m_{tot} have an impact on SP, the identification of the ideal lattice size should be performed on a case-by-case basis, depending on the requirements of each specific application. In this perspective, the proposed modeling approach is ideal for the model-based design of the optimal Cartesian lattice.

4. Conclusions

This work investigates the performance of a latent thermal energy storage system manufactured by 3D printing, consisting in an aluminum Cartesian lattice infiltrated by a paraffin wax. The aim was to accelerate the charging and discharging phases of the device by improving the thermal transport between a heat-transfer fluid, namely water, and the poorly conductive paraffin. The device was tested experimentally considering working conditions representative of low-temperature applications. The results obtained were used to validate a corresponding finite-element model, which was used to further investigate the performance of the manufactured heat storage unit. The device was able to store about 125 kJ of thermal energy in less than 180 s and release them in less than 90 s. The most remarkable figure of merit is the large specific power achieved by the device, approximately 714 ± 17 W kg^{-1} and 1310 ± 48 W kg^{-1} for the charging and discharging process. The device performance remained stable over multiple charging and discharging cycles. Furthermore, the device performance can be further enhanced by optimizing the size of the elementary unit of the Cartesian lattice, which can be achieved relying on the multi-physics model presented in this work. Results show the importance of considering the use of phase change materials in the design of thermal energy storage systems, as latent heat accounted for approximately 35% of the thermal energy stored and released in the tested configuration.

In perspective, the fast charging and discharging cycle of the prototype would be suitable for automotive applications: for example, heat from the cooling radiator of engine could be recovered, stored and then re-used to speed up the cold start phase, which is critical for pollutants production [31]. However, a scaled-up version of the prototype should include a re-design of the thermal insulation layers, for example by means of vacuum containers: the tested wood and wool covers were only intended for the purpose of the performed characterization and model validation.

Summarizing, this work aims at demonstrating the disruptive potential that metal additive manufacturing could have in the thermal energy storage field, thanks to the possibility to rapidly optimize, design and manufacture complex-shaped structures made of thermally-conductive materials.

Statistical analysis

The combined uncertainties of experimental measurements were estimated as [48–50]: $U = k\sqrt{u_A^2 + u_B^2}$, where u_A are the uncertainty components estimated from the statistical analysis of the measured values, u_B are the uncertainty components estimated from a priori information (i.e., calibration, resolution and accuracy of each measuring instrument employed), $k = 2$ is the coverage factor. If the sample size was larger than 30 measurements, the uncertainty components u_A were estimated as the standard deviation of the data set; otherwise, they were estimated as $u_A = 0.5\,|x_{max} - x_{min}|$. All the uncertainty bands or error bars reported in the figures show a $\pm U$ interval.

CRediT authorship contribution statement

Matteo Morciano: Software, Writing – original draft, Writing – review & editing, Validation, Methodology. **Matteo Alberghini:** Software, Writing – original draft, Validation, Methodology. **Matteo Fasano:** Supervision, Formal analysis. **Mariella Almiento:** Investigation. **Flaviana Calignano:** Resources. **Diego Manfredi:** Resources. **Pietro Asinari:** Supervision, Conceptualization, Funding acquisition. **Eliodoro Chiavazzo:** Supervision, Conceptualization, Funding acquisition, Project administration.

Declaration of competing interest

The authors declare that they have no known competing financial interests or personal relationships that could have appeared to influence the work reported in this paper.

Data availability

Data will be made available on request

Acknowledgments

The authors are grateful to the NANOSTEP (La Ricerca dei Talenti, Fondazione CRT – Torino) project. E.C. acknowledges partial support of the Italian National Project PRIN Heat transfer and Thermal Energy Storage Enhancement by Foams and Nanoparticles (2017F7KZWS).

Appendix A. Modeling convection

For the sake of completeness, the device was additionally simulated in the presence of convection within the phase change material. The methodology used for modeling the mushy region, where liquid and solid fraction of material coexist, was based on an apparent analogy between the partially liquid material in the mushy zone and a porous medium, as widely proposed in the literature [51–54]. In other words, the mushy zone was treated as a 'pseudo' porous medium, with porosity equal to the liquid fraction. The latter variable ranges between 0 and 1, as function of the PCM temperature. Therefore, when the material has fully solidified in a computational cell, the porosity becomes zero as well as the velocity. This formulation is also widely used for implementing the well-known enthalpy-porosity method [51–54]. In detail, the momentum equation solved within the PCM domain reads as follows:

$$\rho\frac{\partial \mathbf{v}}{\partial t} = -\nabla p + \mu^{\star}\nabla^2\mathbf{v} + \mathbf{S} + \rho g\,, \tag{A.1}$$

where ρ and $\mathbf{v}$ are the temperature-dependent density and velocity field of the PCM, respectively, $\mu^{\star}$ is the modified PCM viscosity, and $\mathbf{S}$ is a temperature-dependent source term. The last two terms are introduced in the momentum equation to extend its applicability to the mushy region. The source term is defined as $\mathbf{S} = -A(\epsilon)\cdot\mathbf{v}$. Usually, it is assumed that the flow in the mush is governed by the Darcy's Law, namely $\mathbf{v} = -\frac{K}{\mu}\nabla p$ being K the permeability, which is function of the porosity. Then, $A(\epsilon)$ can be described by the widely used Carman–Kozeny equation [51,52] for flow in porous media:

$$A = C_{mush}\frac{1-\epsilon^2}{\epsilon^3+q} \tag{A.2}$$

where q is a small computational constant used to avoid division by zero (here, 10^{-3}), and C_{mush} is the mushy zone parameter, here assumed to be 10^5 (kg m^{-3} s^{-1}), as reported in several studies in the literature. The porosity function $A(\epsilon)$ was used to gradually reduce the velocities from a finite value, when the PCM is liquid, to zero upon complete solidification. Within the solid fraction, the source term $\mathbf{S}$ predominates over all the other terms of the momentum equation, leading to the trivial solution $\mathbf{v} = 0$, therefore granting immobility. In the liquid region, the source term can be neglected with respect to the other terms of the momentum equation, leading to the evaluation of the velocity field only where relevant, therefore reducing the computation cost of the updated model. This ensured that flow was induced only in the liquid fraction within the computational domain, despite solving the moment equation for both fractions, solid and liquid. To achieve convergence in the model, however, it is recommended to additionally modify the viscosity in COMSOL Multiphysics® as [51–54]:

$$\mu^{\star} = \mu_l\left(1 + C\frac{1-\epsilon^2}{\epsilon^3+q}\right) \tag{A.3}$$

where C is a dimensionless parameter with the same numerical value of C_{mush}. The numerical results of the model including convection within the PCM were reported in Fig. A.1. In detail, panel **A** compares the latent and total stored energy obtained including convection in the PCM during charging (dashed and dotted red lines, respectively) with those obtained neglecting convection (black lines). Moreover, panel **B** compares the average outlet temperature of the water during the charging transient when considering (red dots) or neglecting (blue line) convection in the PCM, showing that both models involved no appreciable difference in this outcome.

As can be appreciated from the results reported in the figures, the model neglecting convection in the PCM ensured reliable and reasonable results. Moreover, the assumption of no-convection resulted to be conservative, as it led to higher values of t_{90} and of the related

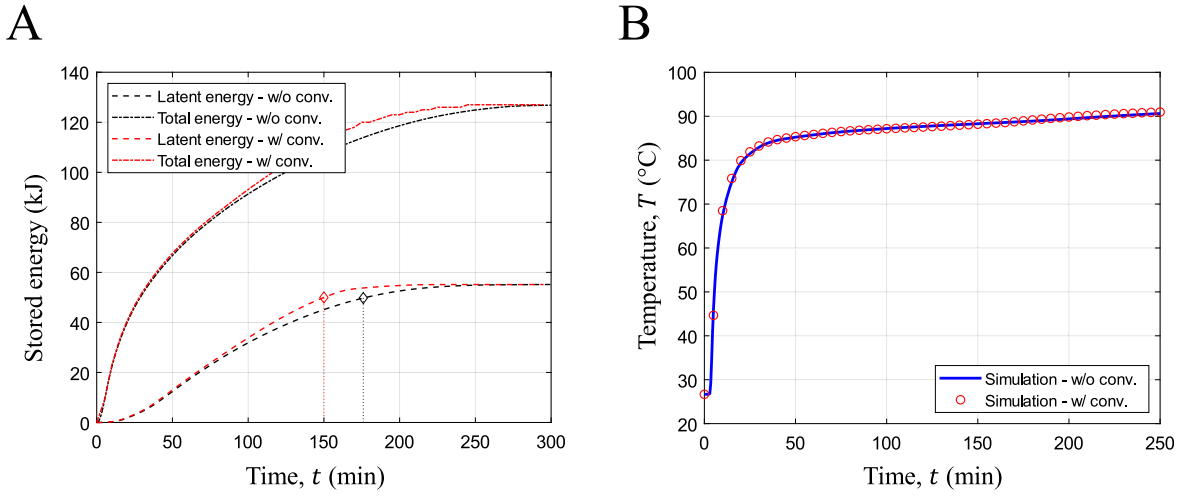

Fig. A.1. Thermal energy storage performance of the device: numerical results. Thermal energy stored (A) and outlet temperature (B) during the charging phase, with (red lines) and without (black or blue lines) convection in the phase change material. (For interpretation of the references to color in this figure legend, the reader is referred to the web version of this article.)

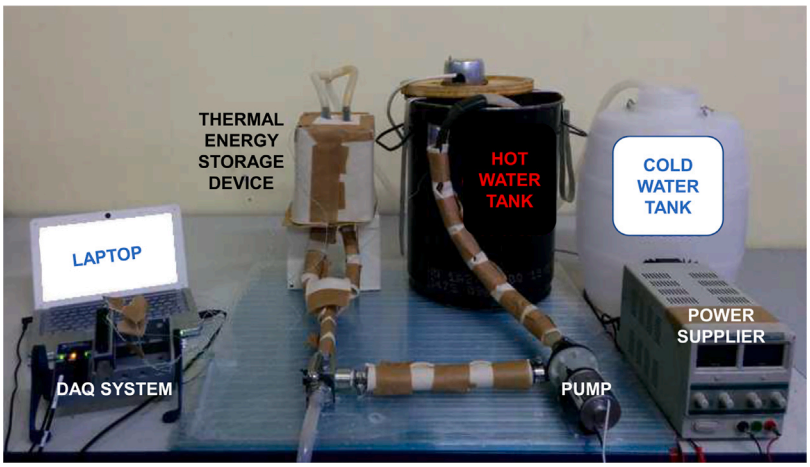

Fig. B.1. Picture of the experimental test bench.

power density SP: including convection, t_{90} and SP were reduced by approximately 14% and 17%, respectively, for the charging phase. On the other hand, the computational cost was found to be significantly different. In detail, the model with convection required a considerably higher computational cost. Its time required amounted to 9 days, 8 h, and 21 min, for a single simulation (Intel i9 vPRO processor, 32 GB RAM); in stark contrast, the convection-free model required approximately 40 h.

Appendix B. Experimental test bench

In Fig. B.1, the experimental test bench is reported. The experimental test bench employed consists of (i) a centrifugal pump with a maximum mass flow rate of 30 l min^{-1}, powered by the reported (ii) power supplier; (iii) the thermally insulated thermal energy storage prototype; (iv) a storage tank with capacity of about 20 l, which was connected to a heater (nominal power of 3 kW) to heat up the water contained (i.e., hot water tank); (v) a storage tank with capacity of about 20 l, which contained water at ambient temperature (i.e., cold water tank); (vi) data acquisition system connected to a laptop; (vii) three-way valve, for the flow regulation.

Appendix C. Temperature distribution

In Fig. C.1, the temperature distribution in the 3D Cartesian metal lattice and in the PCM during the simulated charging process is reported at different time frames.

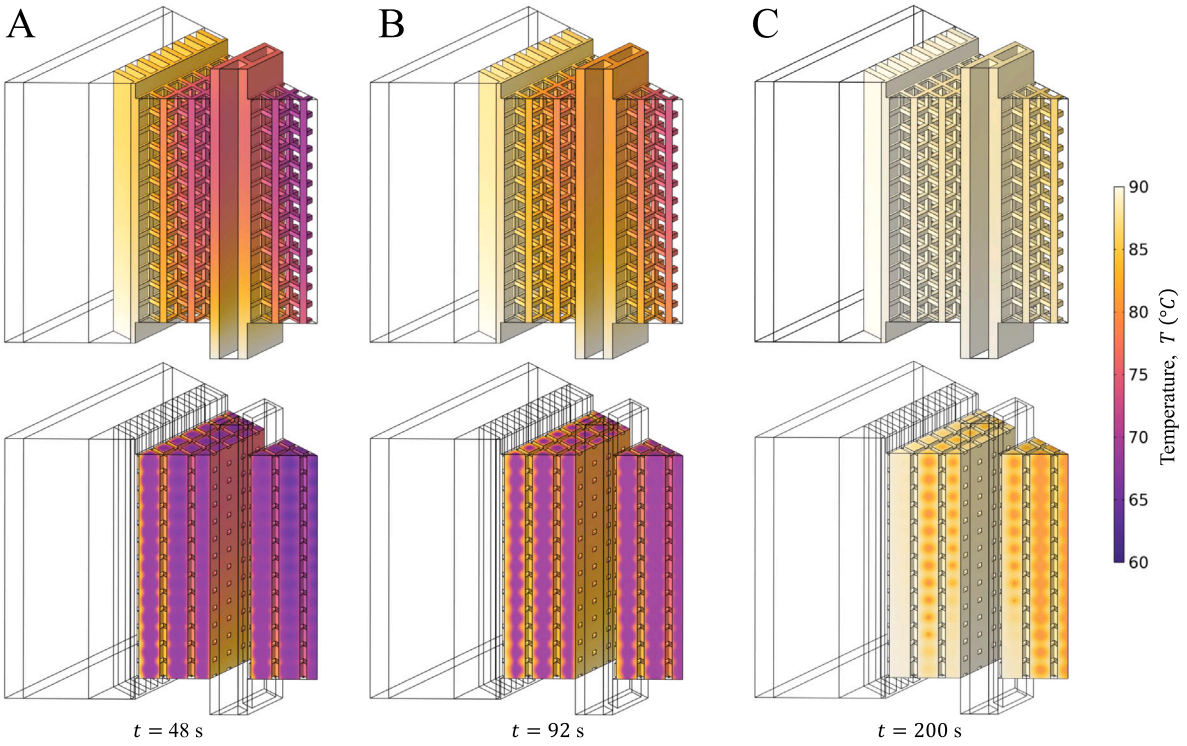

Fig. C.1. Temperature distribution in the 3D Cartesian metal lattice and in the PCM, during the simulated charging process at different time frames.

Appendix D. Supplementary data

Supplementary material related to this article can be found online at https://doi.org/10.1016/j.est.2023.107350.

References

[1] J. Xu, R. Wang, Y. Li, A review of available technologies for seasonal thermal energy storage, Sol. Energy 103 (2014) 610–638.

[2] G. Liu, Z. Du, T. Xiao, J. Guo, L. Lu, X. Yang, K. Hooman, Design and assessments on a hybrid pin fin-metal foam structure towards enhancing melting heat transfer: An experimental study, Int. J. Therm. Sci. 182 (2022) 107809.

[3] G. Liu, T. Xiao, J. Guo, P. Wei, X. Yang, K. Hooman, Melting and solidification of phase change materials in metal foam filled thermal energy storage tank: Evaluation on gradient in pore structure, Appl. Therm. Eng. 212 (2022) 118564.

[4] S. Narayanan, X. Li, S. Yang, H. Kim, A. Umans, I.S. McKay, E.N. Wang, Thermal battery for portable climate control, Appl. Energy 149 (2015) 104–116.

[5] S. Narayanan, H. Kim, A. Umans, S. Yang, X. Li, S.N. Schiffres, S.R. Rao, I.S. McKay, C.A.R. Perez, C.H. Hidrovo, et al., A thermophysical battery for storage-based climate control, Appl. Energy 189 (2017) 31–43.

[6] D. Zhou, C.-Y. Zhao, Y. Tian, Review on thermal energy storage with phase change materials (pcms) in building applications, Appl. Energy 92 (2012) 593–605.

[7] A. Sharma, V.V. Tyagi, C. Chen, D. Buddhi, Review on thermal energy storage with phase change materials and applications, Renew. Sustain. Energy Rev. 13 (2) (2009) 318–345.

[8] G.G. Han, H. Li, J.C. Grossman, Optically-controlled long-term storage and release of thermal energy in phase-change materials, Nature Commun. 8 (1) (2017) 1446.

[9] M.K. Rathod, J. Banerjee, Thermal stability of phase change materials used in latent heat energy storage systems: a review, Renew. Sustain. Energy Rev. 18 (2013) 246–258.

[10] H. Michels, R. Pitz Paal, Cascaded latent heat storage for parabolic trough solar power plants, Sol. Energy 81 (6) (2007) 829–837.

[11] Y. Yuan, X. Cao, B. Xiang, Y. Du, Effect of installation angle of fins on melting characteristics of annular unit for latent heat thermal energy storage, Sol. Energy 136 (2016) 365–378.

[12] S. Hosseinizadeh, F. Tan, S. Moosania, Experimental and numerical studies on performance of pcm-based heat sink with different configurations of internal fins, Appl. Therm. Eng. 31 (17) (2011) 3827–3838.

[13] A.M. Abdulateef, J. Abdulateef, S. Mat, K. Sopian, B. Elhub, M.A. Mussa, Experimental and numerical study of solidifying phase-change material in a triplex-tube heat exchanger with longitudinal/triangular fins, Int. Commun. Heat Mass Transfer 90 (2018) 73–84.

[14] L.F. Cabeza, A. Castell, C. d. Barreneche, A. De Gracia, A. Fernandez, Materials used as pcm in thermal energy storage in buildings: a review, Renew. Sustain. Energy Rev. 15 (3) (2011) 1675–1695.

[15] W.-M. Yan, Y.-H. Siao, A. Kasaeiana, Transient thermal energy storage in partitioned enclosures packed with microencapsulated phase change materials, Int. Commun. Heat Mass Transfer 86 (2017) 253–261.

[16] J. Wei, Y. Kawaguchi, S. Hirano, H. Takeuchi, Study on a pcm heat storage system for rapid heat supply, Appl. Therm. Eng. 25 (17) (2005) 2903–2920.

[17] J. Wang, H. Xie, Z. Xin, Thermal properties of paraffin based composites containing multi-walled carbon nanotubes, Thermochim. Acta 488 (1) (2009) 39–42.

[18] S. Kim, L.T. Drzal, High latent heat storage and high thermal conductive phase change materials using exfoliated graphite nanoplatelets, Sol. Energy Mater. Sol. Cells 93 (1) (2009) 136–142.

[19] A. Sari, A. Karaipekli, Thermal conductivity and latent heat thermal energy storage characteristics of paraffin/expanded graphite composite as phase change material, Appl. Therm. Eng. 27 (8) (2007) 1271–1277.

[20] C. Lin, Z. Rao, Thermal conductivity enhancement of paraffin by adding boron nitride nanostructures: a molecular dynamics study, Appl. Therm. Eng. 110 (2017) 1411–1419.

[21] M. Fasano, M.B. Bigdeli, M.R.V. Sereshk, E. Chiavazzo, P. Asinari, Thermal transmittance of carbon nanotube networks: guidelines for novel thermal storage systems and polymeric material of thermal interest, Renew. Sustain. Energy Rev. 41 (2015) 1028–1036.

[22] M. Li, A nano-graphite/paraffin phase change material with high thermal conductivity, Appl. Energy 106 (2013) 25–30.

[23] C.R. Abujas, A. Jove, C. Prieto, M. Gallas, L.F. Cabeza, Performance comparison of a group of thermal conductivity enhancement methodology in phase change material for thermal storage application, Renew. Energy 97 (2016) 434–443.

[24] B. Buonomo, O. Manca, D. Ercole, S. Nardini, Numerical simulation of thermal energy storage with phase change material and aluminum foam, in: Sixth International Conference on Porous Media and Its Applications in Science, Engineering and Industry, Vol. 11, 2016, pp. 1–6.

[25] P. Zhang, Z. Meng, H. Zhu, Y. Wang, S. Peng, Melting heat transfer characteristics of a composite phase change material fabricated by paraffin and metal foam, Appl. Energy 185 (2017) 1971–1983.

[26] T. Xiao, G. Liu, J. Guo, G. Shu, L. Lu, X. Yang, Effect of metal foam on improving solid–liquid phase change in a multi-channel thermal storage tank, Sustain. Energy Technol. Assess. 53 (2022) 102533.

[27] A. Ribezzo, G. Falciani, L. Bergamasco, M. Fasano, E. Chiavazzo, An overview on the use of additives and preparation procedure in phase change materials for thermal energy storage with a focus on long term applications, J. Energy Storage 53 (2022) 105140.

[28] W. Wu, X. Yang, G. Zhang, X. Ke, Z. Wang, W. Situ, X. Li, J. Zhang, An experimental study of thermal management system using copper mesh-enhanced composite phase change materials for power battery pack, Energy 113 (2016) 909–916.

[29] E. Lohse, G. Schmitz, Experimental analysis of regularly structured composite latent heat storages for temporary cooling of electronic components, Heat Mass Transf. 49 (11) (2013) 1565–1575.

[30] E. Lohse, G. Schmitz, Performance assessment of regularly structured composite latent heat storages for temporary cooling of electronic components, Int. J. Refrig. 35 (4) (2012) 1145–1155.

[31] M. Fasano, L. Bergamasco, A. Lombardo, M. Zanini, E. Chiavazzo, P. Asinari, Water/ethanol and 13x zeolite pairs for long-term thermal energy storage at ambient pressure, Front. Energy Res. 7 (2019) 148.

[32] A. du Plessis, S.M.J. Razavi, M. Benedetti, S. Murchio, M. Leary, M. Watson, D. Bhate, F. Berto, Properties and applications of additively manufactured metallic cellular materials: A review, Prog. Mater. Sci. (2021) 100918.

[33] G. Righetti, G. Savio, R. Meneghello, L. Doretti, S. Mancin, Experimental study of phase change material (pcm) embedded in 3d periodic structures realized via additive manufacturing, Int. J. Therm. Sci. 153 (2020) 106376.

[34] S. Mancin, A. Diani, L. Doretti, K. Hooman, L. Rossetto, Experimental analysis of phase change phenomenon of paraffin waxes embedded in copper foams, Int. J. Therm. Sci. 90 (2015) 79–89.

[35] X. Hu, X. Gong, Experimental and numerical investigation on thermal performance enhancement of phase change material embedding porous metal structure with cubic cell, Appl. Therm. Eng. 175 (2020) 115337.

[36] A. Diani, C. Nonino, L. Rossetto, Melting of phase change materials inside periodic cellular structures fabricated by additive manufacturing: Experimental results and numerical simulations, Appl. Therm. Eng. 215 (2022) 118969.

[37] E. Chiavazzo, L. Ventola, F. Calignano, D. Manfredi, P. Asinari, A sensor for direct measurement of small convective heat fluxes: Validation and application to micro-structured surfaces, Exp. Therm Fluid Sci. 55 (2014) 42–53.

[38] S.D. Burch, T.F. Potter, M.A. Keyser, M.J. Brady, K.F. Michaels, Reducing Cold-Start Emissions By Catalytic Converter Thermal Management, Tech. rep., SAE technical paper, 1995.

[39] F. Calignano, G. Cattano, D. Manfredi, Manufacturing of thin wall structures in alsi10mg alloy by laser powder bed fusion through process parameters, J. Mater Process. Technol. 255 (2018) 773–783.

[40] L. Ventola, F. Robotti, M. Dialameh, F. Calignano, D. Manfredi, E. Chiavazzo, P. Asinari, Rough surfaces with enhanced heat transfer for electronics cooling by direct metal laser sintering, Int. J. Heat Mass Transfer 75 (2014) 58–74.

[41] M. Fasano, L. Ventola, F. Calignano, D. Manfredi, E.P. Ambrosio, E. Chiavazzo, P. Asinari, Passive heat transfer enhancement by 3d printed pitot tube based heat sink, Int. Commun. Heat Mass Transfer 74 (2016) 36–39.

[42] F. Calignano, O.A. Peverini, G. Addamo, L. Iuliano, Accuracy of complex internal channels produced by laser powder bed fusion process, J. Manuf. Process. 54 (2020) 48–53.

[43] A. Ciuffini, A. Scattina, F. Carena, M. Roberti, G. Toscano Rivalta, E. Chiavazzo, M. Fasano, P. Asinari, Multiscale computational fluid dynamics methodology for predicting thermal performance of compact heat exchangers, J. Heat Transfer 138 (7) (2016).

[44] A. Sciacovelli, R. Borchiellini, V. Verda, Numerical Design of Thermal Systems, CLUT, 2013.

[45] Rubitherm technologies gmbh, rt70hc data sheet, 2022, https://www.rubitherm.eu/media/products/datasheets/Techdata_-RT70HC_EN_09102020.PDF, [Online; accessed 14-July-2022].

[46] H. Bjurström, B. Carlsson, An exergy analysis of sensible and latent heat storage, J. Heat Recovery Syst. 5 (3) (1985) 233–250.

[47] A. Roberts, R. Brooks, P. Shipway, Internal combustion engine cold-start efficiency: A review of the problem, causes and potential solutions, Energy Convers. Manage. 82 (2014) 327–350.

[48] BIPM, IEC, IFCC, ILAC, ISO, IUPAC, IUPA, OIML, Evaluation of Measurement Data – Guide To the Expression of Uncertainty in Measurement, Vol. 100, Joint Committee for Guides in Metrology, JCGM, 2008.

[49] M. Alberghini, S.V. Boriskina, P. Asinari, M. Fasano, Characterisation and modelling of water wicking and evaporation in capillary porous media for passive and energy-efficient applications, Appl. Therm. Eng. 208 (2022) 118159.

[50] M. Alberghini, M. Morciano, M. Giardino, F. Perrucci, L. Scaltrito, D. Janner, E. Chiavazzo, M. Fasano, P. Asinari, Textured and rigid capillary materials for passive energy-conversion devices, Adv. Mater. Interfaces 9 (18) (2022) 2200057.

[51] B. Niezgoda-Zelasko, The enthalpy-porosity method applied to the modelling of the ice slurry melting process during tube flow, Procedia Eng. 157 (2016) 114–121.

[52] V.K. Krastev, G. Falcucci, Comparison of enthalpy-porosity and lattice boltzmann-phase field techniques for the simulation of the heat transfer and melting processes in lhtes devices, in: E3S Web of Conferences, Vol. 312, EDP Sciences, 2021, p. 01002.

[53] J. Woodfield, M. Alvarez, B. Gómez-Vargas, R. Ruiz-Baier, Stability and finite element approximation of phase change models for natural convection in porous media, J. Comput. Appl. Math. 360 (2019) 117–137.

[54] C. Reichl, S. Both, P. Mascherbauer, J. Emhofer, Comparison of two cfd approaches using constant and temperature dependent heat capacities during the phase transition in pcms with experimental and analytical results, Processes 10 (2) (2022) 302.